



**HAL**  
open science

## **Spatio-temporal surface soil heat flux estimates from satellite data; results for the AMMA experiment at the Fakara (Niger) supersite**

A. Verhoef, Catherine Oettle, B. Cappelaere, Tom Murray, S. Saux-Picart, Mehrez Zribi, F. Maignan, Nicolas Boulain, J. Demarty, David Ramier

### ► **To cite this version:**

A. Verhoef, Catherine Oettle, B. Cappelaere, Tom Murray, S. Saux-Picart, et al.. Spatio-temporal surface soil heat flux estimates from satellite data; results for the AMMA experiment at the Fakara (Niger) supersite. *Agricultural and Forest Meteorology*, 2012, 154- 155, pp.55-66. 10.1016/j.agrformet.2011.08.003 . ird-00694547

**HAL Id: ird-00694547**

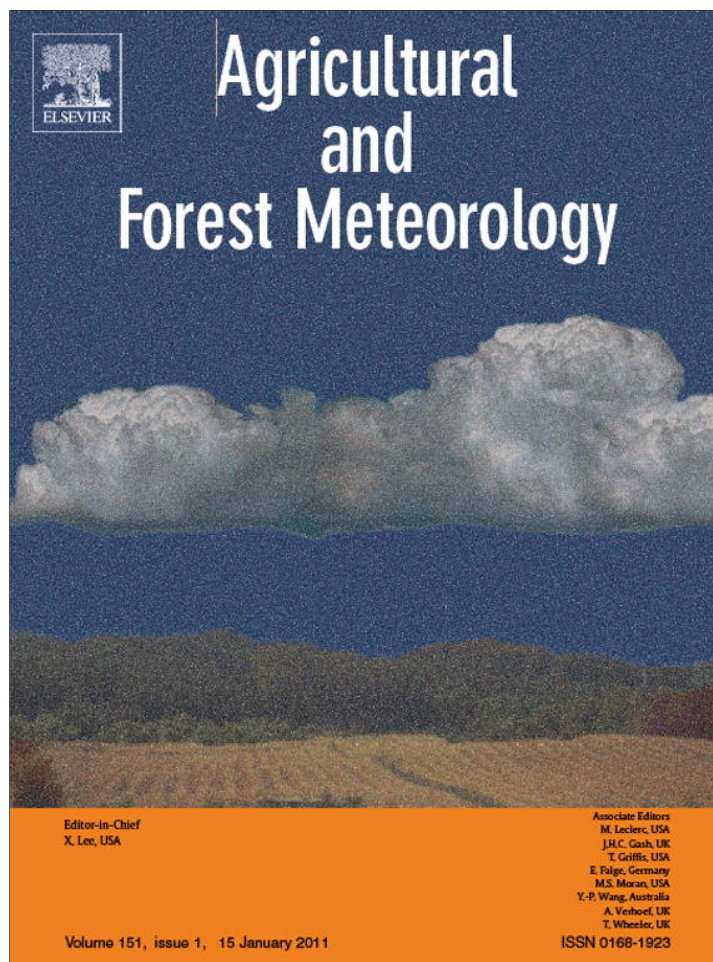
**<https://ird.hal.science/ird-00694547>**

Submitted on 4 May 2012

**HAL** is a multi-disciplinary open access archive for the deposit and dissemination of scientific research documents, whether they are published or not. The documents may come from teaching and research institutions in France or abroad, or from public or private research centers.

L'archive ouverte pluridisciplinaire **HAL**, est destinée au dépôt et à la diffusion de documents scientifiques de niveau recherche, publiés ou non, émanant des établissements d'enseignement et de recherche français ou étrangers, des laboratoires publics ou privés.

Provided for non-commercial research and education use.  
Not for reproduction, distribution or commercial use.



(This is a sample cover image for this issue. The actual cover is not yet available at this time.)

This article appeared in a journal published by Elsevier. The attached copy is furnished to the author for internal non-commercial research and education use, including for instruction at the authors institution and sharing with colleagues.

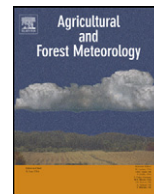
Other uses, including reproduction and distribution, or selling or licensing copies, or posting to personal, institutional or third party websites are prohibited.

In most cases authors are permitted to post their version of the article (e.g. in Word or Tex form) to their personal website or institutional repository. Authors requiring further information regarding Elsevier's archiving and manuscript policies are encouraged to visit:

<http://www.elsevier.com/copyright>

Contents lists available at [SciVerse ScienceDirect](http://www.elsevier.com/locate/agrformet)

# Agricultural and Forest Meteorology

journal homepage: [www.elsevier.com/locate/agrformet](http://www.elsevier.com/locate/agrformet)

## Spatio-temporal surface soil heat flux estimates from satellite data; results for the AMMA experiment at the Fakara (Niger) supersite

Anne Verhoef<sup>a,\*</sup>, Catherine Ottlé<sup>b</sup>, Bernard Cappelaere<sup>c</sup>, Ty Murray<sup>a</sup>, Stephane Saux-Picart<sup>d</sup>, Mehrez Zribi<sup>e</sup>, Fabienne Maignan<sup>b</sup>, Nicolas Boulain<sup>c,f</sup>, Jerome Demarty<sup>c</sup>, David Ramier<sup>g</sup>

<sup>a</sup> The University of Reading, Soil Research Centre, Department of Geography and Environmental Science, Reading, United Kingdom

<sup>b</sup> LSCE/CEA-CNRS, L'Orme des Merisiers Bat 7, 91191 Gif-sur-Yvette, France

<sup>c</sup> IRD, UMR HydroSciences, 911 Avenue Agropolis, BP 64501, 34394 Montpellier Cedex 05, France

<sup>d</sup> Plymouth Marine Laboratory, Prospect Place, The Hoe, Plymouth PL1 3DH, United Kingdom

<sup>e</sup> CESBIO (CNRS/IRD/UPS/CNES), 18, Avenue Edouard Belin, 31401 Toulouse, France

<sup>f</sup> Plant Functional Biology and Climate Change Cluster, P.O. Box 123, Broadway, NSW 2207, Australia

<sup>g</sup> Laboratoire HydroSciences Montpellier, France

### ARTICLE INFO

#### Article history:

Received 11 May 2011

Received in revised form 5 August 2011

Accepted 16 August 2011

#### Keywords:

Land surface temperatures

MSG

Soil heat flux

AMMA

Sahel

### ABSTRACT

This paper describes a method that employs Earth Observation (EO) data to calculate spatiotemporal estimates of soil heat flux,  $G$ , using a physically-based method (the Analytical Method). The method involves a harmonic analysis of land surface temperature (LST) data. It also requires an estimate of near-surface soil thermal inertia; this property depends on soil textural composition and varies as a function of soil moisture content. The EO data needed to drive the model equations, and the ground-based data required to provide verification of the method, were obtained over the Fakara domain within the African Monsoon Multidisciplinary Analysis (AMMA) program. LST estimates ( $3 \text{ km} \times 3 \text{ km}$ , one image  $15 \text{ min}^{-1}$ ) were derived from MSG-SEVIRI data. Soil moisture estimates were obtained from ENVISAT-ASAR data, while estimates of leaf area index,  $LAI$ , (to calculate the effect of the canopy on  $G$ , largely due to radiation extinction) were obtained from SPOT-HRV images. The variation of these variables over the Fakara domain, and implications for values of  $G$  derived from them, were discussed. Results showed that this method provides reliable large-scale spatiotemporal estimates of  $G$ . Variations in  $G$  could largely be explained by the variability in the model input variables. Furthermore, it was shown that this method is relatively insensitive to model parameters related to the vegetation or soil texture. However, the strong sensitivity of thermal inertia to soil moisture content at low values of relative saturation ( $<0.2$ ) means that in arid or semi-arid climates accurate estimates of surface soil moisture content are of utmost importance, if reliable estimates of  $G$  are to be obtained. This method has the potential to improve large-scale evaporation estimates, to aid land surface model prediction and to advance research that aims to explain failure in energy balance closure of meteorological field studies.

Crown Copyright © 2011 Published by Elsevier B.V. All rights reserved.

### 1. Introduction

The surface energy balance describes the energy exchange between the land surface and the atmosphere:

$$R_n = H + LE + G \quad (1)$$

where  $R_n$  is the net radiation,  $H$  is the sensible heat flux,  $LE$  is the latent heat flux, i.e. the evapotranspiration, and  $G$  is the surface soil heat flux (all fluxes in  $\text{W m}^{-2}$ ). A key variable that plays a role in all these fluxes is the land surface temperature, LST.

Recently, determination of the surface soil heat flux,  $G$ , has received renewed attention, predominantly to help explain failure in energy balance closure (e.g. Heusinkveld et al., 2004; Foken, 2008; Jacobs et al., 2008), i.e. the occurrence of a consistent discrepancy between  $R_n$  and  $H + LE + G$ , or rather between  $R_n - G$  (the available energy) and  $H + LE$  (the atmospheric turbulent fluxes), for a particular data set. The main focus of these studies was to draw attention to problems related to the calculation of  $G$  when using in situ sensors, such as the influence of measurement errors and instrument shortcomings on  $G$  estimates (Liebethal et al., 2005; Ochsner et al., 2006, 2007; Sauer et al., 2007), or the effect of latent heat transfer on soil heat flux measurements (Mayocchi and Bristow, 1995; Heitman et al., 2010). Assessment of the degree of energy balance closure is particularly important when

\* Corresponding author. Tel.: +44 118 3786074; fax: +44 118 3786660.

E-mail address: [a.verhoef@reading.ac.uk](mailto:a.verhoef@reading.ac.uk) (A. Verhoef).

evaluating the reliability of energy balance fluxes at FLUXNET sites (<http://www.fluxnet.ornl.gov/fluxnet/>), for example, as these data are used widely by the meteorological research community (e.g. for verification of land surface models, see Blyth et al., 2010).

However, no matter how accurate the estimates of  $G$  from ground-based methods are, a major unresolved problem is the fact that  $G$  obtained by standard in situ methods represents a land surface area of  $<1 \text{ m}^2$  compared to the  $\text{km}^2$  scale associated with  $H$  and  $LE$  flux estimates obtained by the eddy-covariance (Moncrieff et al., 1997) or scintillometry methods (Evans et al., 2010). Large-scale estimates of  $G$  are not only useful for testing of energy balance closure, but also in the context of reliable regional to global evaporation products (e.g. WACMOS, <http://wacmos.itc.nl/>), or WATCH, [www.eu-watch.org](http://www.eu-watch.org)) and of providing verification data for Regional or Global Circulation Models (see e.g. Boone et al., 2009 and Kergoat et al., 2011, in the AMMA framework).

For this reason, over the years researchers have turned their attention on obtaining  $G$  by use of variables that can be obtained from remote sensing, using proximal (Wang and Bras, 1999; Verhoef, 2004; Murray and Verhoef, 2007a,b) to satellite-based Earth Observation (EO) instruments (Bastiaanssen et al., 1998a,b; Tsuang, 2005).

Remotely sensed variables used in these methods generally comprise net radiation, surface temperature, albedo and NDVI (e.g., Choudhury et al., 1987; Kustas et al., 1993; Friedl, 2002; Bastiaanssen et al., 1998a,b; Jacobsen and Hansen, 1999; Santanello and Friedl, 2003). Albedo serves as a proxy for soil moisture content, as this variable strongly affects soil thermal properties. NDVI provides an estimate of vegetation coverage fraction, as, under the same atmospheric driving conditions, vegetation-covered soil will have a smaller soil heat flux than bare soil, due to radiation-extinction by the canopy. A large number of these papers focus on the determination of  $G/R_n$ , from which  $G$  can be derived, provided  $R_n$  is known; experimentally it has been shown that the  $G/R_n$  ratios vary approximately between 0.05 for dense vegetation to 0.3–0.4 for bare soil (e.g. Verhoef, 2004; Murray and Verhoef, 2007b).

Unfortunately, the majority of these approaches are largely empirical, nor are these methods universal. Some of these techniques and their (dis)advantages, were discussed by Murray and Verhoef (2007a,b) and a case was made for replacing these empirical equations with a universal, more physically-based, method based on the Analytical Method (see also Horton and Wierenga, 1983; Verhoef, 2004), which involves a harmonic analysis of surface temperatures and also requires estimates of surface thermal inertia. This method has been tested on the field-scale by Verhoef (2004) for bare soil and by Murray and Verhoef (2007a,b) for vegetated surfaces, using proximal remote sensing to determine surface temperature. Another physically-based method that uses LST (in this case satellite-based) to derive  $G$ , discussed in Tsuang (2005), only considers annual and diurnal variations and no lower-frequency components, so the number of harmonics is much less. It also requires estimates of an effective soil depth, which is hard to obtain, and uses a constant thermal inertia of  $1789 \text{ J m}^{-2} \text{ K}^{-1} \text{ s}^{-1/2}$ , which is unrealistic. Furthermore, this method directly uses skin temperatures at the top of the canopy, but does not correct for the effect of the canopy (see Section 2.1). In Tsuang's paper this caused a discrepancy between the ground fluxes calculated by using radiometric temperatures and those observed at the study sites.

Here, the method derived by Murray and Verhoef (2007a,b), until now used only with proximal LST data, will be tested for a much larger area: the African Monsoon Multidisciplinary Analysis (AMMA; Redelsperger et al., 2006) Fokara domain (approximately  $50 \text{ km} \times 50 \text{ km}$ ) in SW Niger, using satellite remote sensing data. It will allow the Analytical Method to be evaluated for large-scale estimation of  $G$ . The relatively dry and sandy soils of this geographical

area represent a challenging test-bed for this method. Recommendations for its successful use over different surface types and for different climatic regimes will also be made.

## 2. Materials and methods

### 2.1. Calculation of surface soil heat flux from remote sensing data

Calculation of the surface soil heat flux,  $G$ , is performed using the method described by Murray and Verhoef (2007b); from here on referred to as (MV2007b) for vegetated surfaces, as based on Verhoef (2004; method valid for bare soils only). Here, the Analytical soil heat flux method, which is originally based on a harmonic analysis of *below-ground* soil temperatures (Van Wijk and De Vries, 1963; Horton et al., 1983), is employed. However, in this case the harmonic analysis is performed on *surface* temperatures,  $T_s$ , obtained from infrared thermometry (IRT). The following equation was derived by MV2007b (see also Verhoef, 2004):

$$G = \Gamma \sum_{n=1}^M A_n \sqrt{n\omega} \sin \left[ n\omega t + \phi_n + \frac{\pi}{4} \right] = \Gamma J_s \quad (2)$$

where  $\Gamma$  is the thermal inertia,  $M$  ( $=20$ ) is the total number of harmonics used (the use of 20 harmonics should ensure that high frequency temporal fluctuations, e.g. due to temporary cloud cover, are captured satisfactorily),  $A_n$  is the amplitude of the  $n$ th harmonic,  $\phi_n$  is the phase shift of the  $n$ th harmonic,  $t$  is time and  $\omega$  is the angular frequency.  $J_s$  is used to denote the sum of the harmonic terms derived from the timeseries of  $T_s$ , to allow for brevity of notation later on in the manuscript. This equation is considerably less complicated than when using *below-ground* soil temperatures, because all terms containing depth,  $z$ , have disappeared. Verhoef (2004) successfully used Eq. (2) to calculate soil heat fluxes for a bare UK soil. In this study  $\Gamma$  was derived from the nighttime drop in soil surface temperature and the average net radiation received during this period. Note that this approach to calculate  $\Gamma$  cannot be used for vegetated surfaces. For this purpose, Murray and Verhoef (2007a) developed an alternative method (see Eq. (5)).

For vegetated surfaces, calculation of  $G$  with Eq. (2) ideally requires a harmonic analysis of *below-canopy* soil surface temperature, to obtain the shape of the diurnal course of  $G$ , as determined by  $J_s$ . However, when using remote sensing, generally only one single composite (vegetation plus soil) radiometric brightness temperature,  $T_B$ , is available. A new approach was therefore adopted in MV2007b, where a direct relationship was inferred between the sum of the harmonic terms of *below-canopy* soil surface temperatures, i.e.  $J_s$ , and the sum of the harmonic terms of radiometric brightness (composite of soil and canopy) temperatures,  $J_B$ , respectively. The rationale behind this approach was that absolute values of *below-canopy* soil surface temperatures are not required in Eq. (2). Although they can be obtained from remotely observed radiometric temperatures (see e.g. Norman et al., 1995; François et al., 1997; Zhaoliang et al., 2001; Friedl, 2002), this involves simultaneous infrared thermometer (IRT) observations at different viewing angles over homogeneous pixels, which is not currently possible from operational satellite or airborne instruments. Only the relationship between instantaneous and daily averaged temperature readings (used in defining  $A_n$  and  $\phi_n$ ) is important (see MV2007b).

Hence,  $J_B$  was simply altered by a fractional soil cover factor,  $f_s$  (to account for the relative contribution of soil and canopy), to obtain an estimate of  $J_s$ :

$$J_s = \left( \frac{1}{2} f_s(\tau) + \frac{1}{2} \right) J_B \quad (3)$$

This equation was tested for a number of vegetation types and densities in MV2007b. Here,  $f_s(\tau)$  is the fractional soil cover as a

function of instrument (IRT) viewing angle,  $\tau$ ;  $f_s(\tau) = 1.0$  for a surface consisting of entirely bare soil. Values for  $f_s(\tau)$  are calculated from leaf area index,  $LAI$ , and  $\tau$ :

$$f_s(\tau) = e^{[-\beta(LAI/\cos(\tau))]} \quad (4)$$

where  $\beta$  is the radiation extinction coefficient (taken as 0.5, which corresponds to a spherical leaf angle distribution, which is deemed adequate for the canopies under consideration). For MSG-SEVIRI observations over the Sahel,  $\tau$  is assumed 0.

As in MV2007b, remote  $G$  was shifted by 1.5 h to further account for the effect of the canopy, which will dampen and delay the temperature signal, when we compare the soil temperature below the canopy to the surface temperature at the top of the canopy. In theory this shift depends to a certain extent on vegetation structure, and on vegetation density or  $LAI$ . However, MV2007b showed that a single value of phase shift was sufficient for the various canopy types and densities tested in their paper, so for reasons of simplicity and consistency this value was selected also in the current study.

### 2.1.1. Calculation of thermal inertia, $\Gamma$

Eq. (2) also requires an estimate of thermal inertia,  $\Gamma$ . Murray and Verhoef (2007a), from here on referred to as (MV2007a) developed an equation to calculate  $\Gamma$  from soil porosity (which was assumed equal to saturated soil moisture content,  $\theta_*$ ) and an estimate of soil moisture content,  $\theta$ :

$$\Gamma = K_e(\Gamma_* - \Gamma_0) + \Gamma_0 \quad (5)$$

where  $K_e$  is the Kersten number (which depends on the degree of saturation,  $\theta/\theta_*$ ),  $\Gamma_*$  is the maximum value of thermal inertia (at saturation) and  $\Gamma_0$  is the thermal inertia when the soil is air-dry. These authors based their values of  $\Gamma$  (for 11 standard USDA textural classification soils, see Clapp and Hornberger, 1978) on the theoretical definition of this composite thermal soil property:

$$\Gamma = \sqrt{C\lambda} \quad (6)$$

Here,  $\lambda$  is the soil thermal conductivity ( $\text{W m}^{-1} \text{K}^{-1}$ ) and  $C$  is the heat capacity ( $\text{J m}^{-3} \text{K}^{-1}$ ).  $\lambda$  was calculated with the model recently proposed by Lu et al. (2007), and  $C$  from the standard equation (e.g. Van Wijk and De Vries, 1963), which assumes soil is composed of solids, water and air and that  $C$  linearly depends on the volume fractions of these phases, multiplied by their respective heat capacities.

Based on an analysis of the eleven general soil textural types (see Table 1 in MV2007a)  $\Gamma_0$  and  $\Gamma_*$  are given by:

$$\Gamma_0 = -1062.4\theta_* + 1010.8 \quad (7a)$$

$$\Gamma_* = 788.2\theta_*^{-1.29} \quad (7b)$$

For the Kersten number, an amended version of the equation given by Lu et al. (2007) was employed:

$$K_e = \exp \left\{ \gamma \left[ 1 - S_r^{\gamma-\delta} \right] \right\} \quad (8)$$

where  $S_r$  is  $\theta/\theta_*$ ,  $\gamma$  is a soil-texture dependent parameter and  $\delta$  is a shape parameter.

Parameters  $\gamma$  and  $\delta$  were optimised so as to adequately describe the shape of normalised  $\Gamma$ , because the Kersten number in Lu et al. (2007) was used to describe the shape of thermal conductivity (rather than thermal inertia) versus soil moisture content. So in Eq. (8),  $\delta = 2.0$  and  $\gamma = 1.78$  for coarse-textured soils (fraction of sand content,  $FS > 0.8$ ),  $\delta = 1.5$  and  $\gamma = 0.93$  for fine-textured soils ( $FS < 0.4$ ) and  $\delta = 4.0$  and  $\gamma = 3.84$  for medium textured soils, with intermediate  $FS$  values (see MV2007a).

At this point it is worth mentioning that Lu et al. (2009) present an updated version of the MV2007a thermal inertia model. For  $\Gamma_0$  they also use Eq. (7a), but they explicitly define  $\Gamma_*$  as  $\Gamma_* = \sqrt{\lambda_* C_*}$ ,

where the symbol  $*$  again denotes saturation, rather than using Eq. (7b). This caused  $\Gamma_*$  to be slightly higher, at least for the two Chinese silt loam soils presented in their Fig. 3. They used a similar type of equation to represent the shape of the curve (Kersten curve), and determined model-specific parameters  $\varepsilon$  and  $m$  for two groups of soils: 2.95 and 0.16, respectively, for coarse soils ( $FS > 0.4$ ), and 0.60 and 0.71 for fine soils ( $FS < 0.4$ ). The implications, for remote  $G$  estimates, of using this marginally different equation for  $\Gamma$  will be tested in Section 3.3.

### 2.1.2. Overview of method

The method described above to calculate  $G$  from remote sensing requires the following variables: brightness temperature estimates ( $T_B$ , required for the harmonic analysis employed to derive the parameters used in Eq. (2):  $A_n$  and  $\phi_n$ ), soil moisture content,  $\theta$ , to obtain the relative saturation,  $S_r$ , used in Eq. (8), and  $LAI$  needed for calculation of fractional soil coverage,  $f_s$ .

Required parameters comprise soil porosity (i.e. saturated soil moisture content,  $\theta_*$ ) and soil textural information; the fraction of sand,  $FS$ , is required to establish what  $\delta$  and  $\gamma$  values to use in Eq. (8). If values of  $\theta_*$  are not available, pedotransfer functions could be used to derive  $\theta_*$  from texture, see e.g. Cosby et al. (1984). Alternatively, porosity values could be determined for a few choice textural groups (coarse, medium, fine; see also MV2007a).

## 2.2. The study-area: AMMA Fagara domain

The remote sensing data needed to drive the model equations presented in Section 2.1, and the ground-based data needed to provide verification of the method, were obtained in the framework of the African Monsoon Multidisciplinary Analysis (AMMA) program (Redelsperger et al., 2006; <http://www.amma-international.org/>). In this paper we focus on the Fagara domain, which is situated in the south-western part of Niger (Cappelaere et al., 2009); latitude: 13.5–13.9° N, longitude 2.2–2.8° E. A detailed description of the main characteristics of the study area can be found in Cappelaere et al. (2009) and Ramier et al. (2009).

The micrometeorological data, as described in Section 2.4, were gathered during the AMMA-Catch experiment (Lebel et al., 2009) at the Wankama site. Spatio-temporal estimates of  $G$  were calculated using the method described in Section 2.1, for June–October 2005. During this period remote sensing as well as in situ data were available. This period comprises the rainy season, characterised by rainfall events and well-defined dry-downs, thereby offering the opportunity to rigorously test the methodology.

## 2.3. Earth observation data

### 2.3.1. Land surface temperature (LST)

The land surface temperature product (LST for  $3 \text{ km} \times 3 \text{ km}$ , one image  $15 \text{ min}^{-1}$ ) derived from Meteosat Second Generation (MSG)-SEVIRI data and provided by the EUMETSAT-Satellite Application Facility on Land Surface Analysis (Land SAF) has been used to represent values of brightness temperatures,  $T_B$ . Note that these data were averaged to half-hourly values for the harmonic analysis required in Eq. (2). In order to remove remaining cloud-contaminated data not detected by the Land SAF processing, a simple filtering methodology was applied on the LST timeseries. The algorithm, based on smoothing and thresholding techniques, is applied at the pixel scale. It derives from the diagnosis that cloudy data are usually observed at the end of the afternoon and are colder than the expected surface temperature cooling. The methodology comprises three steps: (1) the raw LST signal is smoothed; (2) cloudy data are eliminated by application of a 2K threshold on the signal difference smooth minus raw LST; (3) A final smoothing procedure is applied to the remaining data. This methodology

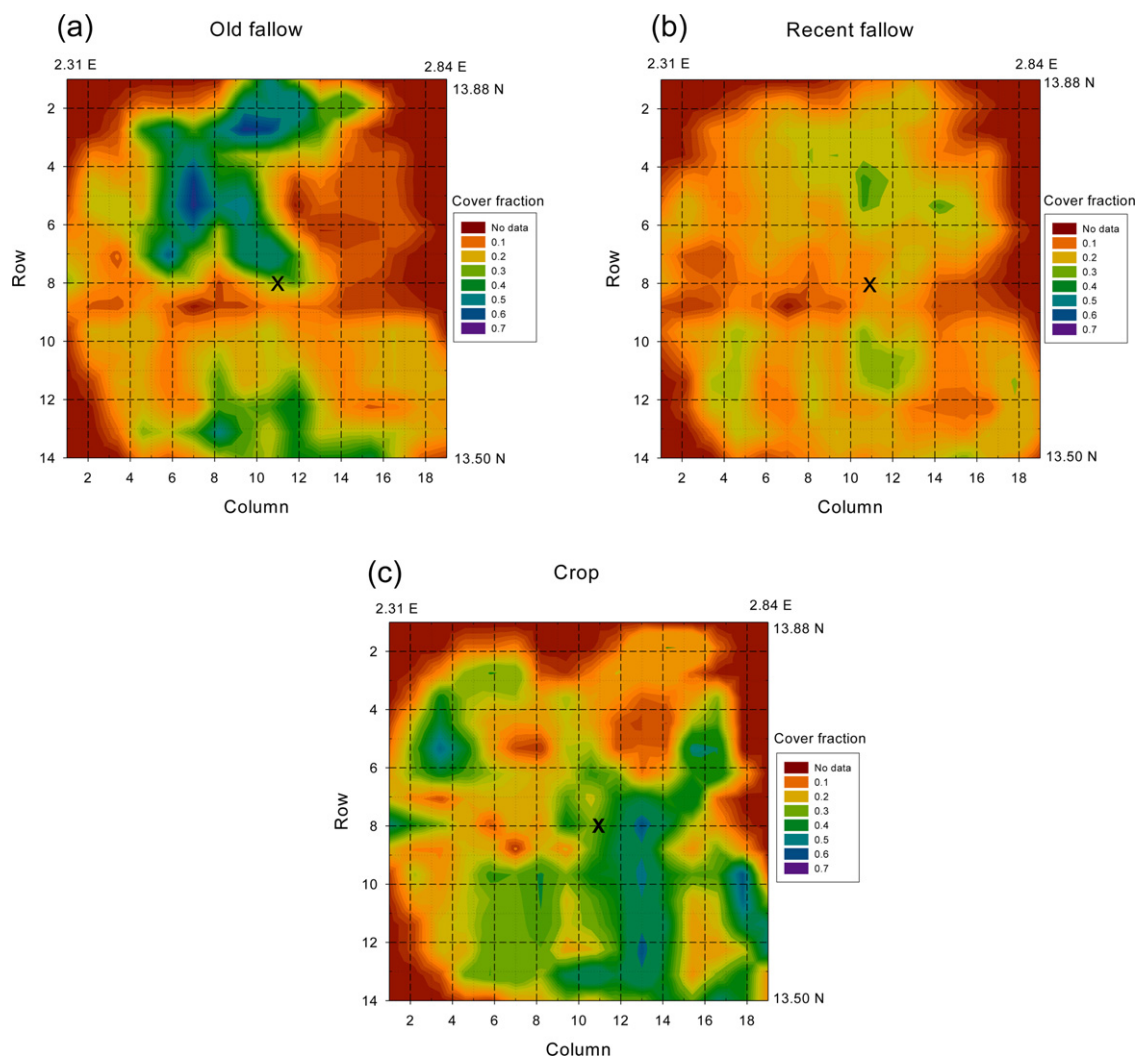


**Fig. 1.** The 3-by-3 km pixel land use cover fraction, over the entire Fakara domain, for the three most important vegetation types: a) old fallow; b) recent fallow and c) crop. The X denotes the pixel where the Wankama experimental sites are situated.

successfully eliminated cloudy data, which were especially prevalent during the rainy season (see Saux-Picart et al., 2009a).

A regular grid of 3 km by 3 km pixels was used to cover the AMMA Fakara domain, an approximately 50 km by 40 km region. The data were provided for 266 grid-boxes (19 columns, 14 rows, see e.g. Figs. 1 and 2), but strictly speaking only 190 of these were within the Fakara domain.

### 2.3.2. Near-surface soil moisture content

Soil moisture estimates were obtained from remote sensing data as described in detail in Zribi et al. (2007). The estimates were based on 15 sets of ASAR/ENVISAT C-band radar data, acquired during the 2004 and 2005 rainy seasons. Simultaneously with radar acquisitions, ground soil moisture measurements were carried out in a large number of test fields. A high correlation was observed between in situ measurements and processed radar data. Images were available in 2005 for 5 July, 7 July, 21 July, 26 July, 9 August, 11 August, 30 August and 15 September.

Soil moisture data were interpolated between these dates, despite the occurrence of some rain events between those dates, because continuous remote  $\theta$  information was not available. This will lead to unavoidable errors in soil moisture estimates, which will be evaluated and discussed in Section 3.3.

### 2.3.3. Land cover mapping

The Fakara region is characterised by dissected plateaus, which are largely covered with tiger bush, a patterned ecosystem consisting of alternating bands of trees or shrubs separated by quasi-bare soils. In the valleys of these plateaus the vegetation is dominated by cultivated fields (mainly millet) and fallow savannahs (Saux-Picart et al., 2009a). A land cover map was derived from SPOT-HRV images (20 m resolution), identifying eight classes. Three classes were identified over the plateaus: bare soils, sparse vegetation and dense vegetation (corresponding to the tiger bush bands), and four classes in the valleys: recent and old fallows, crops and degraded soils; a water class was also considered. The resulting land cover map is presented in Saux-Picart et al. (2009a), Fig. 2.

Bare soils represent the dominant class over the plateaus (17.6%) whereas fallows and crops are dominant in the valleys with respective average fractions of 38.9% and 25.9%. Degraded soils represent 10% of the total area and free water only 0.1%. The Wankama site is in a valley (Saux-Picart et al., 2009a).

### 2.3.4. Seasonal variations in LAI

A set of nine SPOT-HRV images was acquired over the region during the year 2005; seven images were cloudless and covered the

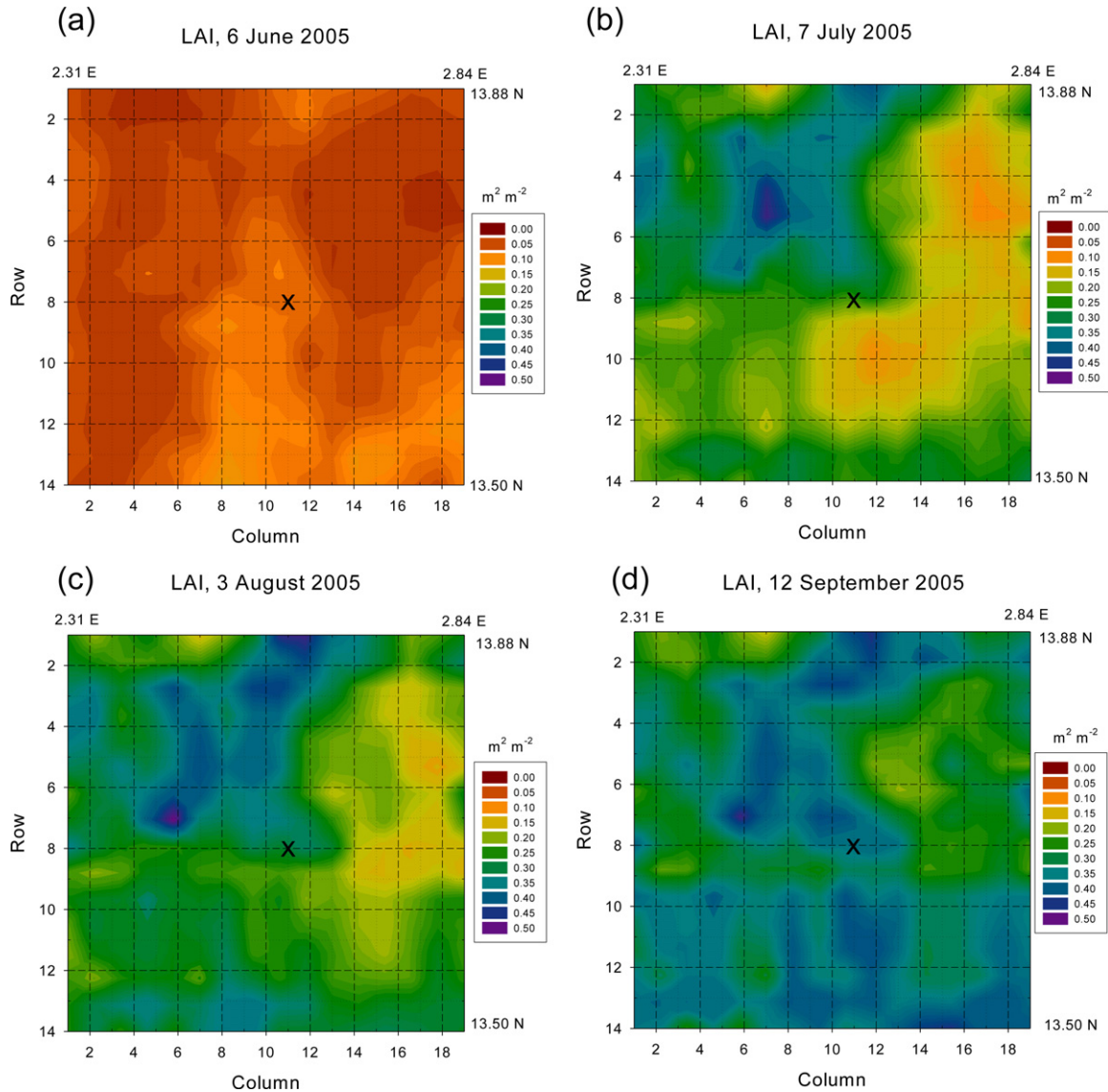


**Fig. 2.** Leaf area index ( $LAI$  in  $m^2 m^{-2}$ ) over the Fakara domain, based on SPOT-HRV images, for: a) 6 June (DOY 157); b) 7 July (DOY 188); c) 3 August (DOY 215); d) 12 September, 2005 (DOY 255).

whole Fakara domain. These images were used to analyse seasonal variations in vegetation growth (dates: 6 June, 13 July, 3 August, 12 September, 28 September, 14 October, and 25 October 2005). The leaf area index,  $LAI$ , was estimated with the neuronal inversion methodology summarised in Baret et al. (2007) and applied in Saux-Picart et al. (2009a).

#### 2.4. In-situ observations at the Wankama site

The soil texture for the Wankama site was determined as <10% clay, <10% silt and 80–90% sand. Hence, because fraction of sand content,  $FS$ , was larger than 0.8, we used  $\delta = 2.0$  and  $\gamma = 1.78$  in Eq. (8). Dry bulk density was estimated by taking undisturbed samples of soil with known volume, and measuring their weight after oven drying for 48 h. At 10 cm, dry bulk density (from which porosity can be calculated) ranged between  $1560\text{--}1650\text{ kg m}^{-3}$  near the millet experimental station and  $1400\text{--}1550\text{ kg m}^{-3}$  near the fallow station. However, it was  $1650\text{--}1810\text{ kg m}^{-3}$  at another fallow plot nearby in the Wankama catchment. Bulk density for both surface types was therefore assumed to be  $1600\text{ kg m}^{-3}$  in all calculations.

Soil physical and meteorological variables were acquired at two micrometeorological sites (fallow savannah and millet) situated in the Fakara domain, close to Wankama village. For both sites, soil volumetric water content was measured using six CS616 water content reflectometers (Campbell Scientific Inc., Logan, USA) at depths of 0.1, 0.5, 1.0, 1.5, 2, and 2.5 m whereas soil temperature was obtained at these same depths with T108 temperature probes (Campbell Scientific Inc., Logan, USA). Shortwave and longwave radiation (downwelling and upwelling), wind speed, air temperature, and humidity were measured with a 30 min time step (see Ramier et al., 2009). Surface temperatures were calculated from the longwave upwelling radiation by inverting the Stefan–Boltzmann equation and assuming an emissivity of 0.95. The temperatures calculated in this way represent a composite (vegetation and soil) surface temperature. Rainfall was measured using a 0.5 mm tipping-bucket rain gauge (Précis Mécanique, Bezons, France).

In-situ  $LAI$  was estimated in the field every two weeks, in  $50 \times 50\text{ m}$  plots in the millet and fallow fields, from hemispherical photographs (Boulain et al., 2009), and time-interpolated by Saux-Picart et al. (2009b).

2.4.1. Soil physical calculations

The Analytical Method, already mentioned in Section 2.1, in this case involving a harmonic analysis of temperatures at depths  $z > 0$ , was used to estimate in situ  $G$ :

$$G_{in-situ}(t) = (C\sqrt{D})_{in-situ} \sum_{n=1}^M \left\{ A_{0n} \sqrt{n\omega} \exp\left(-z\sqrt{n\omega/2D}\right) \sin\left(n\omega t + \varphi_{0n} + \frac{\pi}{4} - z\sqrt{n\omega/2D}\right) \right\} \quad (9)$$

Symbols are as described for Eq. (2). Twenty harmonics obtained from the timeseries of  $T_{soil}$  at  $z = 0.1$  m obtained for the Wankama sites were used; to get the soil heat flux at the surface,  $G$ , involves setting  $z = -0.1$  m in Eq. (9). Knowledge of the harmonic parameters also allowed calculation of surface temperature ( $z = 0$ ), for both sites, from the timeseries of  $T_{soil}$ . For verification purposes, these surface temperatures were compared to the MSG LST product obtained for the pixel in which the Wankama experimental sites are located (see Section 3.1), as well as to the surface temperatures obtained from longwave upwelling radiation (see Section 3.1, Fig. 7).

Eq. (9) also required calculation of thermal diffusivity,  $D$ , and heat capacity,  $C$ , for the layer between 0 and 0.1 m depth. Estimates of  $C$  were obtained using measurements of soil moisture content at 0.1 m depth and a value of dry bulk density ( $1600 \text{ kg m}^{-3}$ ).

$D$  was calculated with the Arctangent Method (Verhoef et al., 1996), using soil temperature measurements,  $T_{soil}$ , at 0.1 and 0.5 m depth. Despite the occurrence of vertical inhomogeneity, it was assumed that this value was also valid for the soil layer between 0 and 0.1 m.

3. Results and discussion

3.1. Model driving data, including in situ verification

3.1.1. Land use distribution

Fig. 1 shows the 3-by-3 km pixel land use coverage fraction, over the entire Fakara domain, for the three most important surface types. The X denotes the pixel where the Wankama micrometeorological field sites are situated. It has the following land use cover fractions: 0.066, 0.045, 0.018, 0.012, 0.334, 0.175, and 0.35, for bare soil plateaus, sparse vegetation plateaus, dense vegetation plateaus, degraded hillslopes, crops, recently converted fallows, and old fallows, respectively. Therefore, about a third of this pixel was covered by crops (during the growing season), and just over half by fallow savannah (deciduous in the dry season). If we ignore the minor land cover components, this means ~40% was covered in crops (millet essentially), the rest by fallow savannah, explaining the rationale behind the selection of the two meteorological field sites. This weighting (a fraction of 0.4 covered by millet and a land cover fraction of 0.6 covered by fallow savannah) will also be used when calculating the verification values of soil heat flux, for example.

Crop cover (Fig. 1c) is generally largest in the bottom right quarter of the Fakara domain (with a pronounced even denser strip for columns 12–14, rows 8–14), whereas the old fallow coverage (see Fig. 1a) is largest in the top centre area of the domain; a clearly defined area (more or less in the shape of the letter X, see also Fig. 2 and related discussion) can be distinguished here. Recently converted fallow is relatively rare, with cover fraction  $< 0.3$  throughout the domain.

3.1.2. Leaf area index

Fig. 2 shows LAI over the Fakara domain. Four dates out of the seven available were selected to illustrate the greening up of the

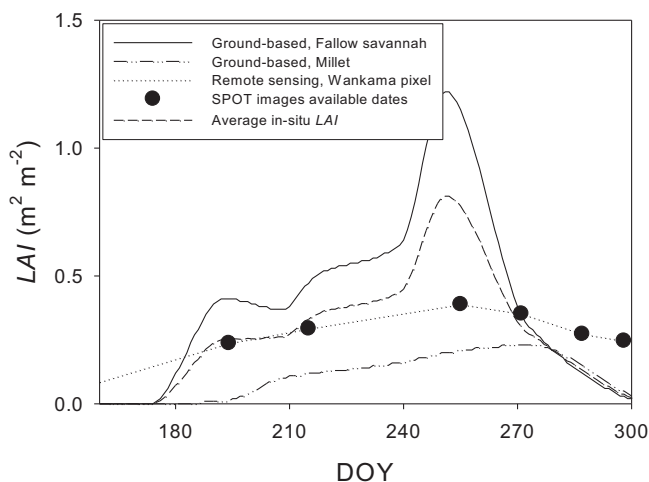


Fig. 3. LAI, as determined using manual methods over the fallow and millet experimental sites, as well as their average, plotted together with the remotely sensed LAI over the pixel representing the Wankama catchment (from SPOT-HRV).

area as a result of precipitation received during the rainy season and the phenological behaviour of the vegetation in the Fakara domain.

According to the SPOT images and related analysis procedure employed (see Section 2.3) LAI was never larger than 0.5. This value compares relatively well to the average of the ground-based LAI values at the Wankama site (presented in Fig. 3 as a function of Day of Year, DOY, together with the individual LAI for savannah and millet; these data are based on interpolations of in situ LAI, determined manually, see Section 2.4).

The timing of the SPOT images unfortunately meant that part of the considerable peak in the 2005 growing season fallow savannah in situ LAI data (around DOY 255, towards the middle of September). According to Fig. 3, SPOT-based LAI may have underestimated in situ LAI between DOY 240–270, but taking into account within-pixel variability, remotely sensed LAI estimates can be considered adequate.

Fig. 2a shows that LAI is  $0.10 \text{ m}^2 \text{ m}^{-2}$  or less on 6 June (DOY 157). However, the arrival of the rains in the Fakara domain at the end of June (i.e. around DOY 180, see Fig. 5, which shows the timeseries of the Wankama rainfall as an illustration of this) causes a greening up, in particular in the X-shaped area where the old fallows dominate (see land cover fraction in Fig. 1a, columns 6–14, rows 1–8), as shown in Fig. 2b. The area of pixels with  $LAI > 0.30$ – $0.35$  increases throughout August and early September; the pattern in Fig. 2d (12 September, DOY 255) roughly reflects the areas covered with old fallows and crops (see Fig. 1a and c). Although the rainfall was obviously spatially variable over the Fakara domain, the Wankama precipitation data shown in Fig. 5 are a good representation of the sequence of wetting up and drying down cycles observed over the domain during the 2005 wet season and how this affects LAI.

Fraction of vegetation cover and type of vegetation (as shown in Fig. 1) will affect the soil heat flux as a result of shading: under the same atmospheric and surface conditions (texture, soil moisture content),  $G$  for a pixel totally or largely occupied by bare soil will be larger than that for a vegetated pixel. Furthermore, the LAI of the vegetation (presented in Fig. 2) will affect the surface soil heat flux (see Eq. (4) in Section 2.1): the denser the vegetation, the smaller  $G$ .

However, vegetation can also have an indirect effect on soil heat flux via its influence on thermal soil properties through soil moisture content. Root water uptake will reduce soil moisture content and hence reduce thermal conductivity. Furthermore, vegetation

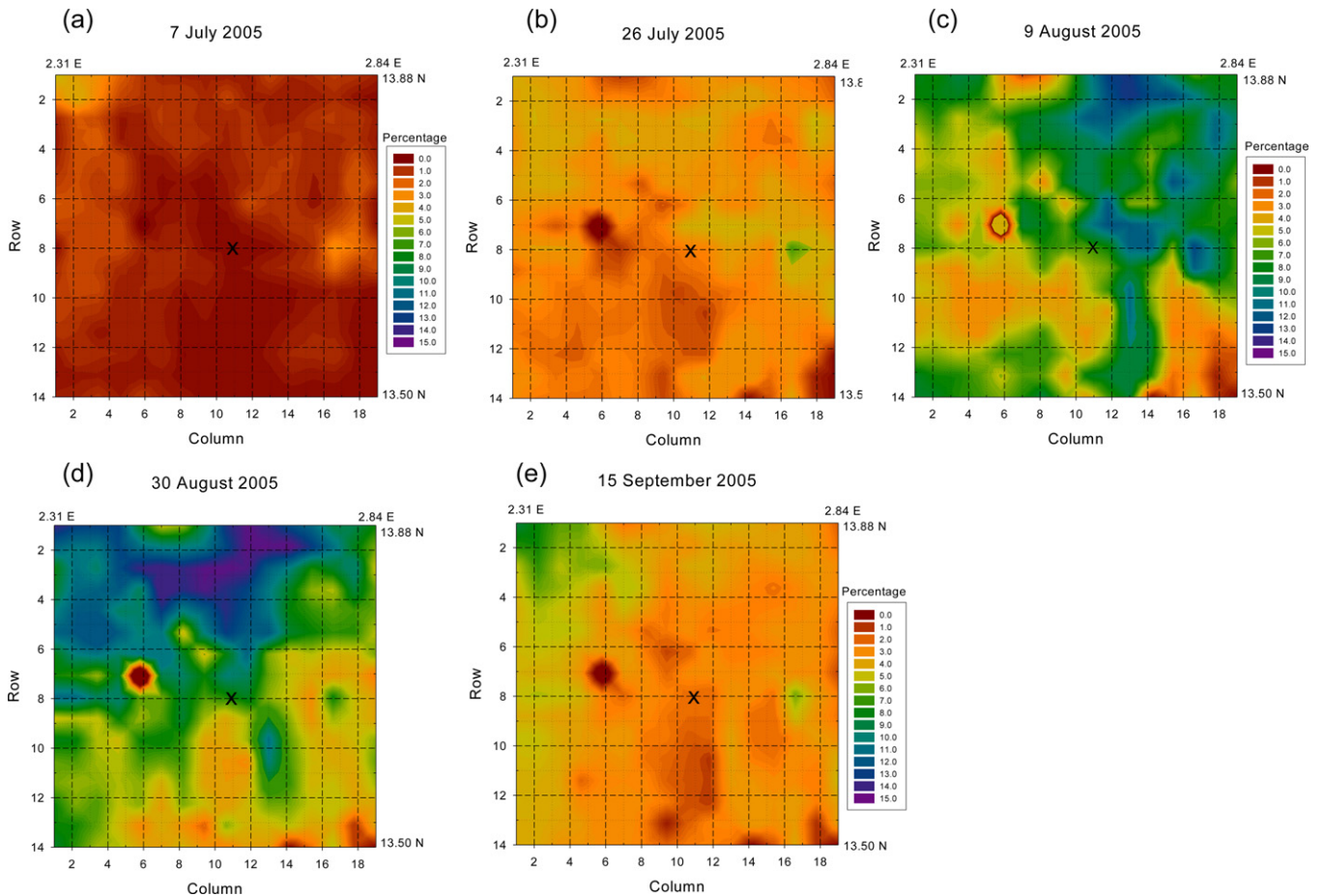


**Fig. 4.** Spatial distribution of near-surface soil moisture content (expressed as a percentage) over the Fakara domain, as derived from ASAR images, for: a) 7 July (DOY 188); b) 26 July (DOY 207); c) 9 August (DOY 221); d) 30 August (DOY 242); e) 15 September (DOY 258), throughout the summer of 2005.

can act as an umbrella and intercept rainwater, part of which may be lost as direct evaporation from the canopy.

### 3.1.3. Soil moisture content

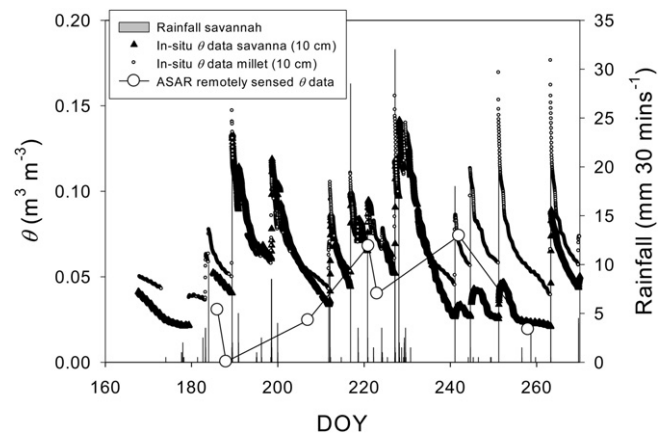
The spatial distribution of ASAR near-surface soil moisture content over the Fakara domain for 5 dates throughout the 2005 growing season is shown in Fig. 4 (expressed as a percentage, i.e.  $\theta$  in  $\text{m}^3 \text{m}^{-3} \times 100$ ). Observed values for ASAR data never exceeded  $0.15 \text{ m}^3 \text{m}^{-3}$  and were at their maximum in late August (Fig. 4d, 30 August, DOY 242). After that, soil moisture rapidly declines (see Fig. 4e) as a result of the high evaporative demand of this area and the peak in vegetation activity (see Figs. 2 and 3). Note a dry anomaly for the pixel represented by column 6, row 7, on all images after 7 July 2005. This is related to an interpolation error where some data points have been removed due to their high surface roughness value (Plateaus) as this causes unreliable ASAR  $\theta$ -values.

Fig. 5 compares the ASAR data (with the actual data values represented by open circles) and the interpolations by a solid line in between these points) for the domain gridbox representing the Wankama site, and the in situ soil moisture content assumed to be representative of this gridbox, for the fallow savannah and millet site, throughout the rainy season. Correspondence between remotely sensed and in situ data is relatively good, although at the start of the rainy season (DOY 186 (5 July), 188 (7 July) and 207 (26 July)) the 3-by-3 km average ASAR data are significantly lower than those measured in situ (up to approximately  $0.04 \text{ m}^3 \text{m}^{-3}$  less). The timing of these ASAR images also seems to coincide with the end of significant dry down periods, which causes Fig. 4a and b to give the impression of drought throughout the Fakara domain, even though

the LAI image (compare e.g. Fig. 2b to Fig. 4a) illustrates a greening up of the area.

During the remainder of the period (i.e. for DOY 221 (9 August), 242 (30 August) and 258 (15 September)) for which ASAR data are available, ASAR  $\theta$  corresponds well with either millet or savannah data (apart from for DOY 223).

Fig. 5 shows that towards the end of the period (after DOY 235), in situ near surface  $\theta$  for millet is considerably larger than that for the fallow savannah, despite the fact that rainfall amounts were



**Fig. 5.** Rainfall recorded at the Wankama savannah site, as well as the in situ (10 cm) and remotely sensed (ASAR) near-surface soil moisture content, between DOY 160 and 270 (9 June–27 September), 2005.

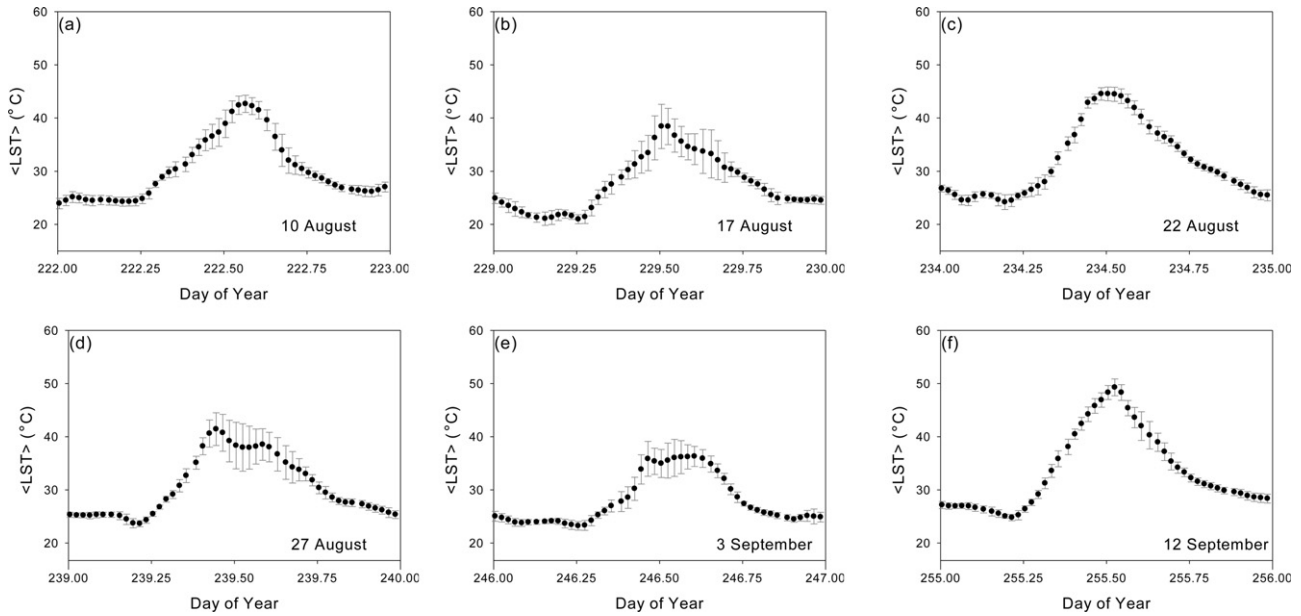


**Fig. 6.** Average land surface temperature (LST, obtained from MSG-data), and its standard deviation, over the Fakara domain for six dates: 10, 17, 22, 27 August (DOY 222, 229, 234 and 239, figures a, b, c, and d, respectively) and 3 and 12 September (DOY 246 and 255, figures e and f, respectively) throughout the 2005 season. Tickmarks are placed at 0.25, 0.5, 0.75 and 1.0 of each DOY (i.e. every 6 h, with e.g. 222.5 represent noon on DOY 222).

very comparable. This may have been caused by the fact that savannah *LAI* increased substantially after DOY 240 (see Fig. 3), most likely as a result of a steep increase in understorey *LAI* (causing a larger root water uptake and hence near-surface soil moisture depletion), whereas the millet crop *LAI* stayed more or less constant. Furthermore, the millet roots would have been located deeper in the soil profile than the fallow understorey layer composed of grasses and forbs. Hence, the savannah understorey may have depleted near surface  $\theta$  more than would have been the case for the millet crop. Also, runoff would have been slightly different at the two sites; because of the propensity of these soils to develop surface crusts and the high intensities of convective rainfall, Hortonian runoff can be very substantial.

ASAR data are particularly sensitive to vertical soil moisture heterogeneity in the first centimeters of the soil profile and this may have caused the discrepancy between the ASAR and in situ data. The high, and relatively variable, evaporation in this region will have induced a high variability in the near-surface soil moisture profile, more so than in humid regions of Europe, for example.

### 3.1.4. Spatiotemporal variation of LSTs

Reliable values of LST, or rather of their amplitude and fluctuations, are crucial in the remote determination of  $G$  (see Eq. (2) and related description); hence they are studied in more detail in this section. In Section 3.3 the relative influence of thermal inertia, and its sensitivity to the variables determining this parameter, will be presented and discussed.

LST will vary throughout the domain, predominantly as a result of spatial variation in vegetation cover fraction (Fig. 1), *LAI* (Fig. 2), and surface soil moisture status,  $\theta$  (Fig. 4), as these variables will have a considerable effect on the fluxes in the energy balance (Eq. (1)), in particular on evapotranspiration. Pixels with bare soil or sparse vegetation are expected to have higher peak temperatures during the day (little or no transpiration and a rapidly declining bare soil evaporation after rainfall) and lower minimum temperatures during the night-time (no insulation by vegetation layer), hence larger diurnal surface temperature amplitudes.

Fig. 6 shows the Fakara domain average LST, from hereon referred to as  $\langle LST \rangle$  and standard deviation,  $\sigma_{LST}$ , for six dates

throughout the season.  $\langle LST \rangle$  varies roughly between 20 °C (night-time) and 50 °C, hence the maximum amplitude (defined as  $(LST_{max} - LST_{min})/2$ ) is approximately 15 °C.

A clear contrast in  $\langle LST \rangle$  amplitude is visible when comparing days such as 17 August (DOY 229), 27 August (DOY 239) and 3 September (DOY 246), that have a less pronounced diurnal curve and large  $\sigma_{LST}$ , with 10 August (DOY 222), 22 August (DOY 234) and 12 September (DOY 255) that show a distinct peak and lower  $\sigma_{LST}$  values.

For DOY 246 (3 September) very low values of  $R_n$  (maximum of 200  $W m^{-2}$ , data not shown) were measured for the Wankama site during the daytime, illustrating this was a cloudy day, most likely throughout the entire domain. By contrast, DOY 255 (12 September) was a perfectly clear day (maximum  $R_n$  of 600  $W m^{-2}$ ), hence the large amplitude in  $\langle LST \rangle$ . Furthermore, this day had low  $\theta$ -values, and generally low spatial variation in  $\theta$  over the Fakara domain (see Fig. 4e) and hence low values of  $\sigma_{LST}$ .

The features presented in Figs. 2, 4 and 6, detailing the spatial variability of *LAI*,  $\theta$  and LST, respectively, will affect the spatiotemporal patterns of soil heat flux  $G$ . This will be discussed in Section 3.2.

### 3.1.5. Surface temperature verification

Verification of the MSG LST estimates was possible via two sets of in situ data: a composite  $T_s$  was derived from longwave upwelling radiation, whereas  $T_{soil}$  at  $z=0$  was calculated from soil temperatures, using the procedures described in Section 2.4.

Fig. 7 shows the comparison between remotely sensed LST (for the Wankama pixel) and in situ (derived from soil temperatures as well as from longwave upwelling radiation) 'LST' for seven days, between early August and the middle of September. Both in situ values are averages, based on the coverage fractions of savannah and millet (0.6 and 0.4, respectively).

The two sets of in situ data ( $T_s$  and  $T_{soil}$  ( $z=0$ )) are very similar, which can be taken as proof of their reliability. It also emphasises the sparsity of the vegetation, i.e. the downward facing long-wave radiometer is mainly sensing soil, i.e. largely looking in between the leaves of the low-*LAI* vegetation.

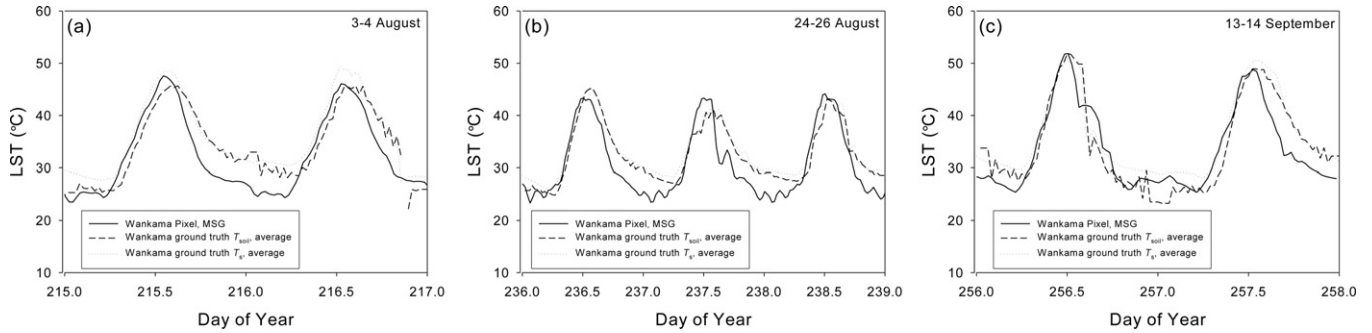


**Fig. 7.** Comparison between LST obtained from MSG and average (40% millet, 60% fallow) in situ (soil) surface temperature derived from 1) a harmonic analysis on soil temperatures at 0.10 m depth. Required thermal properties were derived from soil moisture content measured at 0.10 m and from knowledge of soil textural composition (see Section 2.4) and; 2) composite (soil and vegetation) surface temperature derived from longwave upwelling radiation, for 7 days throughout the season.

Fig. 7 shows that late afternoon and night-time MSG-SEVIRI LST data are generally lower than in situ data, possibly because of the corrections related to cloud-cover. Notwithstanding, the amplitudes of MSG LST, as well as their diurnal shape, are relatively realistic compared to in situ data. This knowledge is important in the context of estimation of  $G$ , and appraisal of its soundness, the ultimate aim of this paper.

### 3.2. Soil heat flux and verification

Fig. 8 shows the domain-average soil heat flux,  $\langle G \rangle$ , as well as its standard deviation  $\sigma_G$  (based on all pixels within the Fakara domain), as calculated with Eq. (2) from remote sensing data. These three plots present 2-day periods that coincide with those shown for Wankama LST in Fig. 7. Furthermore, these dates overlap or are close to the days for which we have remotely sensed (SPOT-HRV) LAI data and ASAR  $\theta$  data.

Soil heat fluxes derived from remote sensing shown in Fig. 8 have a realistic diurnal course, with a peak just before noon, as expected. For each day, we anticipate net heating/cooling of the soil to approximately balance, i.e. the area below the curve reflecting positive  $\langle G \rangle$  to be similar to that below zero; Fig. 8 certainly reflects this. The soil undergoes net cooling during the monsoon season (see Ramier et al., 2009), which causes the integral of negative  $G$  values to be slightly larger than the integral of positive  $G$  values.

Maximum values of  $\langle G \rangle$  are around  $200 \text{ W m}^{-2}$ , minimum values around  $-100 \text{ W m}^{-2}$ . The range of maximum values of  $G$  over the grid varies between 50 and  $250 \text{ W m}^{-2}$ , the minimum values roughly between  $-25$  and  $-150 \text{ W m}^{-2}$  (data not shown). These values are very similar to those presented in e.g. Passerat de Silans et al. (1997) and Verhoef and Allen (2000), as obtained during the HAPEX-Sahel experiment in 1992 in the vicinity of the AMMA Fakara domain.

The values of  $\sigma_G$  vary diurnally;  $\sigma_G$  can be as large as  $\langle G \rangle$  itself. One may expect it to be lowest during the night when  $\sigma_{LST}$  is lowest

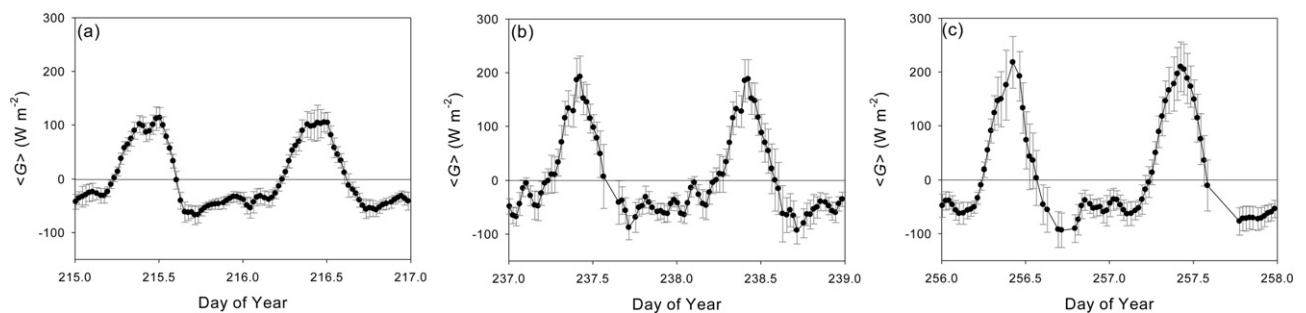
(see Fig. 6 where a clear day-night distinction is visible, especially for days with spatially variable cloud cover such as DOY 229, 239 and 246). However, Fig. 8 shows that  $\sigma_G$  for negative  $\langle G \rangle$  is relatively large during the night and especially during the afternoon, for DOY 237–238. This has to do with the fact that it is not just the spatial variability of  $T_B$  (i.e. LST) that affects  $\sigma_G$ , but also that of  $\theta$  (affecting thermal inertia  $\Gamma$ , see Fig. 10). The contribution of  $\Gamma$  (and hence the effect of its spatial variability on  $G$ ) compared to  $J_s$  is relatively large during the night.

Fig. 9 compares the remote surface soil heat flux for the Wankama pixel and the average in situ soil heat flux derived by the method described in Section 2.4.  $G_{in-situ}$  and  $G_{remote}$  compare relatively well, especially towards the middle (DOY 237–239) and end (DOY 256–258) of the period under consideration (DOY 214–258, before and after this time-span there were gaps in the LST data; the remote Analytical Method was only used for days when all 48 half-hours were available).

The discrepancy between  $G_{in-situ}$  and  $G_{remote}$  for DOY 215–216 is most probably linked to a larger landscape heterogeneity at the beginning of the vegetation growing season. Indeed, we are comparing  $G$ -fluxes that are representative of areas with completely different sizes ( $<1 \text{ m}^2$  compared to  $9 \text{ km}^2$ ), so that the effect of small-scale variability may have caused  $G_{in-situ}$  to be atypical during this earlier part of the season, when vegetation was particularly sparse.

Other reasons may also explain the discrepancies observed between  $G_{in-situ}$  and  $G_{remote}$  in Fig. 9a. The values of in situ  $G$  depend on the harmonic analysis of  $T_{soil}$  at 0.10 m, and on the thermal properties thermal diffusivity,  $D$ , and heat capacity,  $C$ . Values of  $D$  and  $C$  could have been overestimated because of the fact that soil moisture sensors were installed at the same depth as the thermistors (0.1 m), rather than at 0.05 m depth, for example, to be more representative of the layer between 0 and 0.10 m.

$G_{remote}$  could have been underestimated because of  $\theta$  estimated from ASAR being much lower than in situ  $\theta$  (and hence  $\Gamma$  being



**Fig. 8.** Domain average diurnal course of  $G$  estimated with Eq. (2), for three 2-day periods throughout the season. Error bars denote standard deviation.

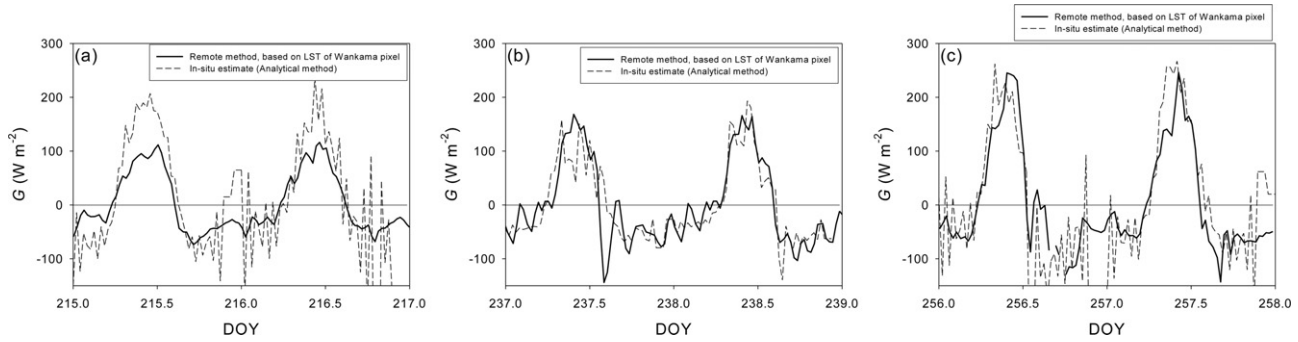


**Fig. 9.** A comparison of the diurnal soil heat flux calculated with Eq. (2) (the remote Analytical Method, using MSG-SEVIRI land surface temperatures) for the Wankama pixel (3 by 3 km<sup>2</sup>) and an in situ estimate of  $G$  (at the Wankama meteorological site) obtained from the in situ Analytical Method (Eq. (9)). In-situ  $G$  represents an average (40% millet, 60% fallow).

too low). Fig. 5 shows that this was not the case; ASAR  $\theta$  interpolated between DOY 207 and DOY 221 (to give the values for DOY 215–216) matches rather well with in situ  $\theta$ .

Also, Fig. 3 shows that  $LAI_{remote}$  was close to average in situ  $LAI$  and therefore most likely represented a realistic value. Therefore, the reason for the comparatively large discrepancy between  $G_{in-situ}$  and  $G_{remote}$  for DOY 215–216, other than being caused by larger landscape heterogeneity, is not immediately clear.

Finally, note that in situ  $G$ -values are much more temporally variable; this is a general feature of the in situ Analytical Method. Soil heat flux plates were installed at the Wankama site, but their data were not used because adequate information to calculate heat storage above the plates was not available.

The remote method generally provides a much smoother signal, especially during the night. This is the result of the pixel size of the temperature measurement: the spatial integration over the kilometeric pixel scale compensates the small-scale temperature fluctuations, driven by the turbulent atmospheric flow, which are measured at the local site.

### 3.3. Sensitivity of $G$ to model input variables and parameters

#### 3.3.1. Effect of soil thermal inertia

$\Gamma$  will impact on absolute  $G$ -values in a linear fashion (it is a straight multiplication factor in Eq. (2)). Fig. 10a shows how sensitive  $\Gamma$  is to  $\theta$ , especially at low  $\theta$ -values, as is the case for the AMMA Fakara domain. The curve representing the MV2007a model is calculated using parameter values characteristic for the sandy soils in the Fakara domain.

Fig. 10a highlights that it crucially important to use reliable estimates of EO-based  $\theta$  when calculating  $\Gamma$ . Note, however, that for soils with a less sandy texture,  $\Gamma$  is not so strongly dependent on  $\theta$  (see MV2007a). The curve in Fig. 10a represents the most extreme case; the dry, sandy Fakara catchment therefore provides a rigorous test case for our method. In wetter climates, especially for soil types of a finer texture, an error in  $\theta$  would have a much smaller effect on  $G$ .

The interpolation of the ASAR  $\theta$  data between the available dates (see large open circles in Fig. 5) will have caused a considerable error (especially when rainfall occurrences took place in between the ASAR observations), which would have affected  $\Gamma$  and hence  $G$ . It is therefore recommended to use remotely sensed  $\theta$  data with as high a temporal resolution as possible.

In Fig. 10a we also briefly explore the effect of a different  $\Gamma$  parameterisation (that of Lu et al., 2009, as described briefly in Section 2.1.1). Fig. 10a shows that differences between both models are very small and that remote  $G$ -estimates are unlikely to be affected by choice of thermal inertia model.

As the MV2007a (as well as the Lu et al. (2009) method for that matter) method to calculate  $\Gamma$  relies on texture estimates from soil maps and derivation of soil physical parameters (i.e.  $\theta^*$ ) from pedo-transfer functions, dependent on these texture estimates, Fig. 10b illustrates the implications of a 10% relative error in  $\theta^*$ , or in fraction of sand, FS.

The effect of  $\theta^*$  on  $\Gamma$  increases as  $\theta$  increases, because  $\Gamma^*$  is more affected than  $\Gamma_0$  (a power function compared to a linear equation, see Eqs. (7a) and (7b)). At the mid-value of the range of soil moisture

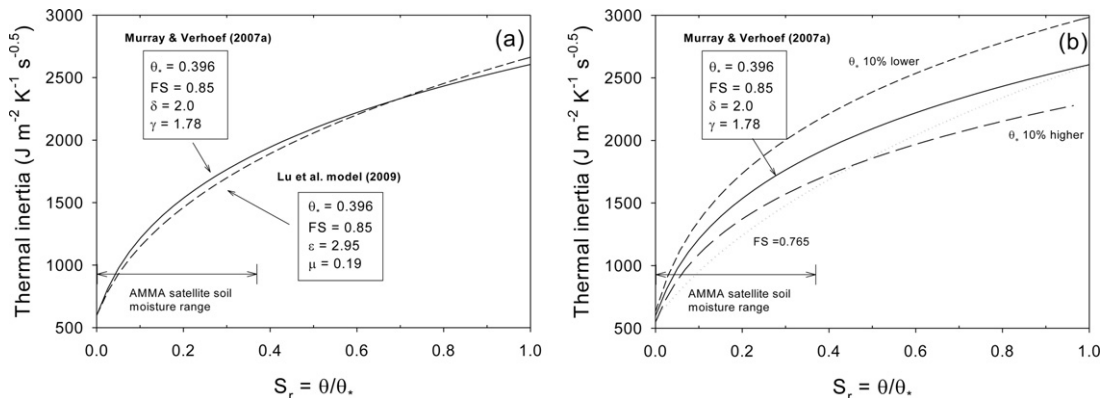


**Fig. 10.** (a) Thermal inertia as a function of relative saturation, as calculated by the model described by Murray and Verhoef (2007a) (i.e. from Eqs. (5), (7) and (8) in this paper), and as derived from the equations presented in Lu et al. (2009); (b) Thermal inertia as a function of relative saturation, as calculated by MV2007a, calculated using the standard soil parameter configuration for the Fakara domain, as well as with a 10% increase or decrease in  $\theta^*$ , or a 10% decrease in fraction of sand (FS; this affects the soil-texture dependent parameter and shape parameter in Eq. (8)).

contents observed over the Fakara domain, the relative increase or decrease in  $\Gamma$  would have been 10–12% and hence a 10–12% change in  $G$  would have occurred.

A 10% relative decrease in sand content (from  $FS=0.85$  to  $0.765$ ) would have brought the Fakara soils just into the medium-textured soil grouping, thereby changing  $\delta$  to 4.0 and  $\gamma$  to 3.84. The curve representing this configuration is shown in Fig. 10b by the dotted line. This would have decreased  $\Gamma$  values, and hence  $G$ , in the Fakara  $\theta$ -range by about 15–20%. Most soils, however, will fall unequivocally within the coarse ( $FS>0.8$ ), medium-textured, or fine-textured ( $FS<0.4$ ) categories.

### 3.3.2. Effect of LAI and canopy extinction coefficient on $J_S/J_B$

Finally, the ratio  $J_S/J_B$  was calculated as a function of LAI, for the range of values found over the Fakara domain ( $0-0.75 \text{ m}^2 \text{ m}^{-2}$ , see Fig. 3;  $0-0.5 \text{ m}^2 \text{ m}^{-2}$  for LAI derived from SPOT images and up to  $0.75 \text{ m}^2 \text{ m}^{-2}$  found for the average in situ LAI values), and three different values of canopy extinction coefficient ( $\beta=0.3, 0.5$  and  $0.7$ ;  $\beta$  was assumed to be 0.5 over the Fakara domain); data not shown. For these LAI values  $J_S/J_B$  ranged (in a linear fashion) between 1.0 and 0.75 (for  $\beta=0.7$ ;  $J_S/J_B$  was higher for lower  $\beta$ -values). It appeared that an absolute error of  $0.10 \text{ m}^2 \text{ m}^{-2}$  in LAI at e.g.  $LAI=0.25 \text{ m}^2 \text{ m}^{-2}$  would only cause an error in  $J_S/J_B$ , and hence in  $G$ , of around 3% (for  $\beta=0.7$ ). This error was even less for smaller  $\beta$  values. The relatively small sensitivity of  $G$  to  $\beta$ , LAI and viewing angle,  $\tau$ , was also illustrated in MV2007b, which underlines the robustness of this method.

## 4. Conclusions

This paper presents a physically-based method (the Analytical Method, based on harmonic analysis of land surface temperature, LST) that allows spatiotemporal estimates of surface soil heat flux,  $G$ , to be determined from remotely sensed variables and an estimate of soil texture. Variables required are surface temperature, leaf area index and near-surface soil moisture content. In this case these were obtained from MSG-SEVIRI LST, SPOT-HRV and ASAR data over the AMMA Fakara domain. The scale of  $G$  estimates is largely determined by the resolution and frequency with which the surface temperature is available; for MSG-SEVIRI LST data this is  $3 \text{ km} \times 3 \text{ km}$  and every 15 min.

The approach requires a substantial amount of input, but the advantage is that the method is robust, universal and ensures a reliable diurnal course of  $G$ , unlike existing methods that derive  $G$  from net radiation and NDVI or albedo, with the latter two serving as proxies of vegetation coverage and soil moisture content. We encourage those research communities that require large-scale model verification or that provide evaporation products derived from the energy balance (see Eq. (1),  $LE=R_n - H - G$ ) to test our method.

Furthermore, with higher resolution EO data becoming more widely available, this method will also be more successful at providing 'field-scale' estimates of  $G$ , compared to methods that derive  $G$  from in situ soil physical equipment, as these have a footprint of  $<1 \text{ m}^2$  only. We postulate that this will generally improve energy balance closure.

Note that that this method requires diurnal data, which can only be obtained from geostationary instruments. The spatial resolution in the thermal infrared for these instruments may reach 300 m in the near future, which is close to field-scale (approximately 100 m). This opens up the opportunity of using EO radiometers and down-scaling techniques to obtain estimates of  $G$  at scales equal to or smaller than field-scale.

## Acknowledgements

The data used in this study were obtained as part of the AMMA programme (Based on a French initiative, AMMA was built by an international scientific group and is currently funded by a large number of agencies, especially from France, UK, US and Africa. It has been the beneficiary of a major financial contribution from the European Community's Sixth Framework Research Programme. Detailed information on scientific coordination and funding is available on the AMMA International web site, <http://www.amma-international.org>), as well as the French ECCO-PNRH "Eau et végétation au Niger" project and the AMMA-Catch observation system ([www.amma-catch.org](http://www.amma-catch.org)). The assistance with data-collection of the IRD team in Niamey is gratefully acknowledged. We thank EUMETSAT-SAFLAND for providing the LST data. We are grateful to Pier Luigi Vidale for optimising the Fortran modelling code.

## References

- Baret, F., Hagolle, O., Geiger, B., Bicheron, P., Miras, B., Huc, M., Berthelot, B., Nino, F., Weiss, M., Samain, O., Roujean, J.L., Leroy, M., 2007. LAI, fAPAR and FCover CYCLOPES global products derived from VEGETATION, part 1: principles of the algorithm. *Remote Sens. Environ.* 110, 275–286.
- Bastiaanssen, W.G.M., Menenti, M., Feddes, R.A., Holtslag, A.A.M., 1998a. The Surface Energy Balance Algorithm for Land (SEBAL): Part 1 formulation. *J. Hydrol.* 212–213, 198–212.
- Bastiaanssen, W.G.M., Pelgrum, H., Wang, J., Ma, Y., Moreno, J., Roerink, G.J., Van Der Wal, T., 1998b. The Surface Energy Balance Algorithm for Land (SEBAL): Part 2 validation. *J. Hydrol.* 212–213, 213–229.
- Blyth, E., Gash, J., Lloyd, A., Prior, M., Weedon, G., Shuttleworth, J., 2010. Evaluating the Jules land surface model energy fluxes using Fluxnet data. *Bull. Am. Meteorol. Soc.* 11, 509–519.
- Boone, A., de Rosnay, P., Balsamo, G., Beljaars, A., Chopin, F., Decharme, B., Delire, C., Ducharme, A., Gascoïn, S., Grippa, M., Guichard, F., Gusev, Y., Harris, P., Jarlan, L., Kergoat, L., Mougïn, E., Nasonova, O., Norgaard, A., Orgeval, T., Ottlé, C., Pocard-Leclercq, I., Polcher, J., Sandholt, I., Saux-Picart, S., Taylor, C., Xue, Y., 2009. The AMMA Land Surface Model Intercomparison Project (ALMIP). *Bull. Am. Meteorol. Soc.* 90, 1860–1880.
- Boulain, N., Cappelare, B., Ramier, D., Issoufou, H.B.A., Halilou, O., Seghieri, J., Guillemain, F., Gignoux, J., Timouk, F., 2009. Towards an understanding of coupled physical and biological processes in the cultivated Sahel – 2. Vegetation and carbon dynamics. *J. Hydrol.* 375 (1–2), 190–203.
- Cappelare, B., Descroix, L., Lebel, T., Boulain, N., Ramier, D., Laurent, J.-P., Le Breton, E., Mamadou, I., Boubkraoui, S., Bouzou Moussa, I., Favreau, G., Issoufou, H.B.A., Nazoumou, Y., Quantin, G., Chaffard, V., Ottlé, C., 2009. The AMMA-Catch experiment in the cultivated Sahelian area of south-west Niger – investigating water cycle response to a fluctuating climate and changing environment. *J. Hydrol.* 375 (1–2), 34–51.
- Choudhury, B.J., Idso, S.B., Reginato, J.R., 1987. Analysis of an empirical model for soil heat flux under a growing wheat crop for estimating evaporation by an infrared-temperature based energy balance equation. *Agric. For. Meteorol.* 39, 283–297.
- Clapp, R.B., Hornberger, G.M., 1978. Empirical equations for some soil hydraulic properties. *Water Resour. Res.* 14, 601–604.
- Cosby, B.J., Hornberger, G.M., Clapp, R.B., Ginn, T.R., 1984. A statistical exploration of the relationships of soil moisture characteristics to the physical characteristics of soils. *Water Resour. Res.* 20, 682–690.
- Evans, J.G., McNeil, D.D., Finch, J.F., Murray, T., Harding, R.J., Verhoef, A., 2010. Evaporation measurements at kilometre scales determined using two-wavelength scintillometry. In: *Proceedings of the BHS Third International Symposium: Role of Hydrology in Managing Consequences of a Changing Global Environment*, 19–23 July 2010, Newcastle University, Newcastle upon Tyne, UK, pp. 794–799.
- Foken, T., 2008. The energy balance closure problem: an overview. *Ecol. Appl.* 18, 1351–1367.
- François, C., Ottlé, C., Prévot, L., 1997. Analytical parameterization of canopy directional emissivity and canopy directional radiance in the thermal infrared. Application on the retrieval of soil and foliage temperatures using two directional measurements. Part 1: Theory. *Int. J. Remote Sens.* 18, 2587–2621.
- Friedl, M.A., 2002. Forward and inverse modelling of land surface energy balance using surface temperature measurements. *Remote Sens. Environ.* 79, 344–354.
- Heitman, J.L., Horton, R., Sauer, T.J., Ren, T., Xiao, X., 2010. Latent heat in soil heat flux measurements. *Agric. For. Meteorol.* 150, 1147–1153.
- Heusinkveld, B.G., Jacobs, A.F.G., Holtslag, A.A.M., Berkowicz, S.M., 2004. Surface energy balance closure in an arid region: role of soil heat flux. *Agric. For. Meteorol.* 122, 21–37.
- Horton, R., Wierenga, P.J., Nielsen, D.R., 1983. Evaluation of methods for determining the apparent thermal diffusivity of soil near the surface. *Soil Sci. Soc. Am. J.* 47, 25–32.
- Horton, R., Wierenga, P., 1983. Estimating the soil heat flux from observations of soil temperature near the surface. *Soil Sci. Soc. Am. J.* 47, 14–20.

- Jacobs, A.F.G., Heusinkveld, B.G., Holtslag, A.A.M., 2008. Towards closing the surface energy budget of a mid-latitude grassland. *Boundary-Layer Meteorol.* 126, 125–136.
- Jacobsen, A., Hansen, B.U., 1999. Estimation of the soil heat flux/net radiation ratio based on spectral vegetation indexes in high-latitude Arctic areas. *Int. J. Remote Sens.* 20, 445–461.
- Kergoat, L., Grippa, M., Baille, A., Eymard, L., Lacaze, R., Mougín, E., Ottlé, C., Pelletier, T., Polcher, J., de Rosnay, P., Roujean, J.-L., Sandholt, I., Taylor, C.M., Zin, I., Zribi, M., 2011. Remote sensing of the land surface during the African Monsoon Multidisciplinary Analysis (AMMA). *Atmos. Sci. Lett.* 12, 129–134.
- Kustas, W.P., Daughtry, C.S.T., van Oevelen, P.J., 1993. Analytical treatment of the relationships between soil heat flux/net radiation ratio and vegetation indices. *Remote Sens. Environ.* 46, 319–330.
- Lebel, T., Cappelaeere, B., Galle, S., Hanan, N., Kergoat, L., Levis, S., Vieux, B., Descroix, L., Gosset, M., Mougín, E., Peugeot, C., Seguis, L., 2009. AMMA-CATCH studies in the Sahelian region of West-Africa: an overview. *J. Hydrol.* 375 (1–2), 3–13.
- Liebethal, C., Huwe, B., Foken, T., 2005. Sensitivity analysis for two ground heat flux calculation approaches. *Agric. For. Meteorol.* 132, 253–262.
- Lu, S., Ren, T., Gong, Y., Horton, R., 2007. An improved model for predicting soil thermal conductivity from water content at room temperature. *Soil Sci. Soc. Am J.* 71, 8–14.
- Lu, S., Ju, Z., Ren, T., Horton, R., 2009. A general approach to estimate soil water content from thermal inertia. *Agric. For. Meteorol.* 149, 1693–1698.
- Mayocchi, C.L., Bristow, K.L., 1995. Soil surface heat flux: some general questions and comments on measurements. *Agric. For. Meteorol.* 75, 43–50.
- Moncrieff, J.B., Massheder, J.M., De Bruin, H., Elbers, J., Friborg, T., Heusinkveld, B., Kabat, P., Scott, S., Soegaard, H., Verhoef, A., 1997. A system to measure surface fluxes of momentum, sensible heat, water vapour and carbon dioxide. *J. Hydrol.* 188–189, 589–611.
- Murray, T., Verhoef, A., 2007a. Moving towards a more mechanistic approach in the determination of soil heat flux from remote measurements. I. A universal approach to calculate thermal inertia. *Agric. For. Meteorol.* 147, 80–87.
- Murray, T., Verhoef, A., 2007b. Moving towards a more mechanistic approach in the determination of soil heat flux from remote measurements. II. Diurnal shape of soil heat flux. *Agric. For. Meteorol.* 147, 88–97.
- Norman, J.M., Kustas, W.P., Humes, K.S., 1995. Source approach for estimating soil and vegetation energy fluxes in observations of directional radiometric surface temperature. *Agric. For. Meteorol.* 77, 263–293.
- Ochsner, T.E., Sauer, T.J., Horton, R., 2006. Field tests of the soil heat flux plate method and some alternatives. *Agron. J.* 98, 1005–1014.
- Ochsner, T.E., Sauer, T.J., Horton, R., 2007. Soil heat storage measurements in energy balance studies. *Agron. J.* 99, 311–319.
- Passerat de Silans, A., Monteny, B.A., Lhomme, J.P., 1997. The correction of soil heat flux measurements to derive an accurate surface energy balance by the Bowen ratio method. *J. Hydrol.* 188–189, 453–465.
- Ramier, D., Boulain, N., Cappelaeere, B., Timouk, F., Rabanit, M., Lloyd, C.R., Boubkraoui, S., Métayer, F., Descroix, L., Wawrzyniak, V., 2009. Towards an understanding of coupled physical and biological processes in the cultivated Sahel – 1. Energy and water. *J. Hydrol.* 375 (1–2), 204–216.
- Redelsperger, J.L., Thorncroft, C., Diedhiou, A., Lebel, T., Parker, D., Polcher, J., 2006. African monsoon multidisciplinary analysis (AMMA): an international research project and field campaign. *Bull. Am. Meteorol. Soc.* 87, 1739–1746.
- Santanello, J.A., Friedl, M.A., 2003. Diurnal covariation in soil heat flux and net radiation. *J. Appl. Meteorol.* 42, 851–862.
- Sauer, T.J., Ochsner, T.E., Horton, R., 2007. Soil heat flux plate: Heat flow distortion and thermal contact resistance. *Agron. J.* 99, 304–310.
- Saux-Picart, S., Ottlé, C., Decharme, B., Andre, C., Zribi, M., Perrier, A., Coudert, B., Boulain, N., Cappelaeere, B., Descroix, L., Ramier, D., 2009a. Water and energy budgets simulation over the AMMA-Niger super-site spatially constrained with remote sensing data. *J. Hydrol.* 375, 287–295.
- Saux-Picart, S., Ottlé, C., Perrier, A., Decharme, B., Coudert, B., Zribi, M., Boulain, N., Cappelaeere, B., Ramier, D., 2009b. SEtHyS\_Savannah: a multiple source land surface model applied to Sahelian landscapes. *Agric. For. Meteorol.* 149, 1421–1432.
- Tsuang, B.-J., 2005. Ground heat flux determination according to land skin temperature observations from in-situ stations and satellites. *J. Hydrometeorol.* 6, 371–390.
- Van Wijk, W.R., De Vries, D.A., 1963. Periodic temperature variations in a homogeneous soil. In: Van Wijk, W.R. (Ed.), *Physics of plant environment*. North-Holland, Amsterdam, pp. 103–143.
- Verhoef, A., 2004. Remote estimation of thermal inertia and soil heat flux for bare soil. *Agric. For. Meteorol.* 123, 221–236.
- Verhoef, A., Van den Hurk, B.J.J.M., Jacobs, A.F.G., Heusinkveld, B.G., 1996. Thermal soil properties for a vineyard (EFEDA-I) and a savanna (HAPEX-Sahel) site. *Agric. For. Meteorol.* 78, 1–18.
- Verhoef, A., Allen, S.J., 2000. A SVAT scheme describing energy and CO<sub>2</sub> fluxes for multi-component vegetation: calibration and test for a Sahelian savannah. *Ecol. Model.* 127, 245–267.
- Wang, J., Bras, R.L., 1999. Ground heat flux estimated from surface soil temperature. *J. Hydrol.* 216, 214–226.
- Zhaoliang, L., Stoll, M.P., Zhang, R., Jia, L., Zhongbo, S., 2001. On the separate retrieval of soil and vegetation temperatures from ATSR Data. *Sci. China D* 44, 97–111.
- Zribi, M., Saux-Picart, S., André, C., Descroix, L., Ottlé, C., Kallel, A., 2007. Soil moisture mapping based on ASAR/ENVISAT radar data over a Sahelian region. *Int. J. Remote Sens.* 28, 3547–3565.